EXPERIMENTS ON AEROTHERMAL AND AERODYNAMIC LOADS OF ROTATING CYLINDRICAL BODIES IN HYPERSONIC FLOW

Patrick M. Seltner, Armin Weiss[1]*, Sebastian Willems, Ali Guelhan*

German Aerospace Center (DLR)
Supersonic and Hypersonic Technologies Department of the Institute of Aerodynamics and Flow Technology
Linder Hoehe, 51147 Cologne, Germany

ABSTRACT

Aero-thermodynamic effects occurring during the re-entry of rotating cylindrical bodies into the atmosphere are analysed in this study. Two test series were performed in the DLR's hypersonic wind tunnel H2K to investigate the aerothermal and aerodynamic loads, with the latter being tested in free flight. As a result, the experiments have shown that the rotation of the body leads to an averaging of the surface temperatures and the flight trajectory between the extremes. In the free-flight tests, a three-dimensional motion behaviour was observed due to the initially forced rotation. This behaviour is attributed to torque-induced precession and not to rotation-induced aerodynamic effects for the investigated configurations.

Index Terms— Re-entry trajectory, High-speed aerodynamics, Aerothermal loads, Hypersonic wind tunnel, Free-flight technique, Infrared thermography

1. INTRODUCTION

The mitigation and avoidance of space debris is becoming increasingly relevant, as the number of objects in Earth orbits is growing disproportionately with increasing rocket launches and new satellite constellations [1]. Remaining space objects, especially in low Earth orbit, pose a critical threat to upcoming space flights and active satellites due to the risk of collision. For this reason, ESA's new Space Debris Mitigation Guidelines aim to reduce the residence time after end-of-life and to lower on-ground casualty risk caused by space debris [2]. ESA's "Design for Demise" (D4D) approach is becoming increasingly relevant in order to develop standards that guarantee the complete and safe demise of next-generation spacecraft. In this context, it is important to investigate the rotational effect of re-entering objects with respect to demisability, since they can begin to tumble after the separation from the main spacecraft. Re-entry analysis tools are also becoming more important to make the prediction of impact footprints and thus the casualty risk assessment more accurate in order to protect people and property from harm. In doing so, the experimental database and modelling capabilities for aero-thermodynamic effects that occur during the re-entry into the atmosphere are limited, in particular with regard to the influence of rotating objects. On this account, the aerothermal and aerodynamic loads of concave and convex bodies at flight-relevant rotational velocities are analysed in two test series for the present work. Thereby, both right circular cylinders and cylinders with cavities in the base and lateral surface are analysed, which are intended to represent generative bodies for propellant tanks and rocket engines.

A literature review showed that stationary cylinders in hypersonic flow fields are a well-documented research object regarding the aerodynamic loads (e.g. [3, 4, 5, 6, 7]). The aerodynamic force and moment coefficients of a cylinder with an aspect ratio of 2 in a wide range of body inclinations were determined in an earlier work [8]. In contrast, just a few researches are made on the aerothermal loads of a cylinder assuming an equilibrium boundary layer (e.g. [4, 9, 5, 7]). These authors point out a strong dependence of the Reynolds number on the flow field, especially on the heat flux distribution. Moreover, Rees et al. observed high heat flux near corners and edges by performing infrared (IR) thermography on cubes [10].

For the aerothermal test series, experiments with stationary and forced-rotating cylindrical bodies were successfully carried out in the Hypersonic Wind Tunnel Cologne (H2K) at the DLR. For this purpose, a model support system was developed that allows a change in the model's angle of attack and rotational frequency. Three different cylindrical models were studied at a free-stream Mach number of 7 with subcritical and supercritical Reynolds numbers for different parameter variations such as the rotational frequency, the direction of rotation and the angle of attack. The surface temperatures were measured with a calibrated infrared camera system of three synchronously recording IR cameras from different perspectives. Schlieren videography was used to capture the flow topology.

For the aerodynamic test series, free-flight tests with initially forced-rotating cylindrical bodies were also successfully performed in the H2K test facility. The advanced

[1] currently at Institute of Propulsion Technology, German Aerospace Center (DLR), Cologne

free-flight technique with an electromagnetic dropping mechanism prevents aerodynamic disturbances caused by a sting or a wind tunnel balance. In these tests, the cylindrical models were tested at Mach 7 under various initial conditions such as angle of attack, rotational frequency and direction of rotation. Six-degrees-of-freedom (6DoF) motion data were measured non-intrusively using a state-of-the-art stereo-tracking measurement technique. At the same time, schlieren videography was used to visualise the flow topology. A comprehensive post-processing routine was used to determine velocities, accelerations and aerodynamic coefficients from the time-resolved positions and orientation angles of the measurement data.

2. EXPERIMENTAL MODELS & METHODS

Two test series were performed in H2K, whereby two different experimental setups with partially different instrumentation were applied. However, the geometries in both test series were the same.

2.1. Hypersonic Wind Tunnel Cologne (H2K)

Both test series were carried out in the Hypersonic Wind Tunnel Cologne H2K, which is located at the Supersonic and Hypersonic Technologies Department of DLR. This wind tunnel is an intermittently operating blowdown facility for maximum reservoir temperatures of 1000 K and fixed design Mach numbers of 5.3, 6.0, 7.0, 8.0, 8.7 and 11.2. At the nozzle exit, the diameter is 600 mm, while the axially symmetrical homogeneous core flow has an average diameter of about 420 mm. In the core flow, the maximum deviation of total pressure is 5%. Additional details on H2K are available in [11].

In each test, the operating conditions of the facility, such as the reservoir pressure p_0 and the reservoir temperature T_0, were gauged in the H2K's settling chamber at a sampling rate of 50 Hz. The reservoir pressure was measured with an absolute pressure transducer of the UNIK 5000 series GE Druck that has an overall accuracy of ±2.8 kPa in the measurement range between 250 kPa and 5500 kPa. A thermocouple type K class 1 from MTB Sensor-Technik with an overall accuracy of ±1.5 K was used for the measurement of reservoir temperature.

For the present work, two nominal test conditions were defined using the same wind tunnel nozzle. These test conditions are summarised in Table 1, in which the free-stream Mach number Ma_∞, the free-stream dynamic pressures q_∞ and the unit free-stream Reynolds numbers Re are specified. Thereby, TC2 was used for both the free-flight and aerothermal tests.

Table 1. Nominal test conditions

	Ma_∞	p_0 [kPa]	T_0 [K]	q_∞ [Pa]	Re [$\frac{10^6}{m}$]
TC1	7.1	2400	600	18913	9.9
TC2	7.0	480	600	3981	2.0

2.2. Model design

Three cylindrical geometries were used for both test series: a right circular cylinder, a cylinder with a parabolic axial-symmetric cavity in the lateral surface (namely dogbone) and a cylinder like the dogbone with an additional parabolic axial-symmetric cavity in both base surfaces (namely nozzle). The aspect ratio is 2 for all bodies. For the model modification of the cavity in the lateral surface, the maximum cavity depth is 60% of the model radius and the cavity length is 60% of the model length. For the cavities in the base areas of the nozzle body, the maximum cavity depth is 35% of the model length and the maximum cavity radius is 70% of the model radius.

For the aerothermal tests, hollow test articles were manufactured out of uncoated poly-ether-ether-ketone (PEEK). PEEK is a commonly used material for IR thermography, for which emissivity data in the IR spectrum are available. The models have a length of 200 mm and their edges are rounded with a radius of 5 mm. The wall thickness of the hollow test articles is 25 mm and the arithmetic average roughness of the surface is 0.8 µm.

For the aerodynamic tests, magnetic species of steel were used for the models, which have a nominal length of 100 mm. The actual properties of the models, including a coating for stereo tracking, are presented in Table 2 with the diameter d , the length l, the mass m and the transverse inertia I_{yy}.

Table 2. Actual model properties

Geometry	d [mm]	l [mm]	m [kg]	I_{yy} [$\frac{kgm^2}{10^3}$]
Cylinder	49.99	100.03	1.536	1.521
Dogbone	50.08	100.15	0.971	1.294
Nozzle	50.05	100.02	0.714	0.880

2.3. Instrumentation

For both test series, high-speed schlieren videography was used with a single-path Z-type setup as in [12] to characterise the flow field around the test objects. A 1000 W xenon arc lamp was used for illumination. A high-speed camera model from the Photron FASTCAM series was used for image recording, which was set to the full resolution of 1024 × 1024 pixels. The frame rate of the camera was set to 1 kHz and 3 kHz, respectively.

A high-speed stereo-tracking system based on the detection of marker points was applied for the free-flight tests, which determines the time-resolved position and orientation of the test object in 3D space. Two Photron FASTCAM SA-X2 model 1080K were used for the synchronously recording cameras. The cameras were set to the full 1024 × 1024 pixels resolution at a frame rate of 12 kHz. Each camera was outfitted with a 24-mm-focal-length lens ensuring the observation of a measurement volume of about 600 × 600 × 600 mm. To ensure sufficient illumination, each camera was equipped with four 86 W plus four 38 W high-power LEDs on a capacitive cooling ring mounted concentrically on the optical window of the protective box. To guarantee a highly accurate measurement, a standardised calibration was performed before each test series under ambient condition, resulting in a calibration deviation of 3 μm. Data processing was conducted as in [8] to determine the aerodynamic force and moment coefficients based on the three positions in streamwise (x), spanwise (y) and vertical (z) direction as well as the roll (φ), pitch (ϑ) and yaw (ψ) angles.

Infrared thermography with three synchronously recording IR cameras were used in the aerothermal test series to measure the surface temperature of around three quarters of the entire lateral surface. These are the IRCAM VELOX 1310k SM, the InfraTec ImageIR 8380 and the IRCAM EQUUS 327k L, whereby the former two are mid-wave infrared (MWIR) cameras and the latter is a long-wave infrared (LWIR) camera. The cameras were set to a frame rate of 100 Hz, whereby the MWIR cameras exhibit an effective frame rate of 50 Hz as they used two integration times. The cameras were enveloped in protective box to prevent an overheating due to the surrounding vacuum in the test section. For the optical access to the boxes, calcium fluoride windows were used for the MWIR cameras and a zinc selenide window for the LWIR camera to ensure high transmission in the respective IR spectrum. Calibrations were used to determine the transmittance of the windows using a black body and the emissivity of the PEEK models. This paper primarily deals with the results of the measurement with the IRCAM Velox 1310k SM, which features a 1280 × 1024 pixels resolution with a NETD of less than 25 mK. The overall uncertainty of this IR camera is ±1 K or ±1%. It was equipped with a 50-mm-focal-length lens.

2.4. Experimental setup of aerothermal test series

Figure 1 depicts the PEEK model in the H2K's test section at an angle of attack (AoA) of $\alpha = 90°$ in the main frame and $\alpha = 80°$ in the top right corner. The model was in the schlieren path with its centre of gravity (CoG) on the nozzle's centre line and its rotation axis parallel to the gravity. Regarding the positioning of the IR cameras, the IRCAM Velox 1310k SM and IRCAM EQUUS 327k L were placed on the left and right side of the nozzle, while the InfraTec ImageIR 8380 was located on the downstream side of the schlieren path next to the diffuser. Thereby, the IR cameras had an angular displacement of roughly 90° to each other with an overlapping field of view. In most of the tests, the rotation was clockwise (CW), as the maximum heat fluxes are expected in the region of the stagnation point, which in this case is shifted in the direction of the rotation where two IR cameras are placed. To enable forced rotation and AoA adjustment in the range of ±20°, the cylinder is supported by a shaft as part of a rotating arm. A stepping motor with a step angle of 1.8° and rotational frequencies of up to 30 Hz was used as the rotational drive, which transmits the torque via the shaft with radial bearings.

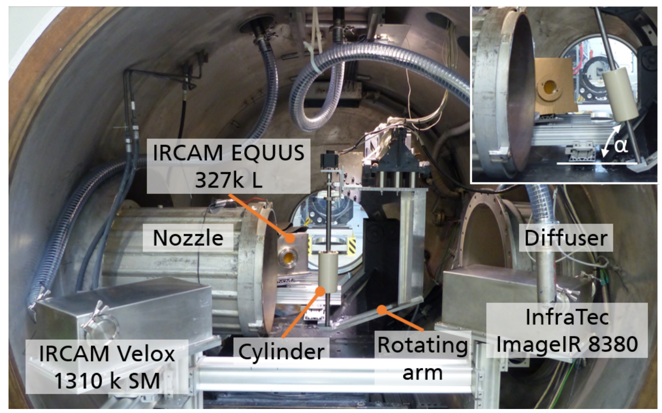

Fig. 1. Experimental setup with infrared thermography in H2K's test section

2.5. Experimental setup of aerodynamic test series

Figure 2 shows the experimental setup in the H2K's test section for fully free-flying test objects by the use of the free-flight technique with an electromagnetic dropping mechanism. This technique has already been used successfully in several studies with single or multiple blunt bodies according to [13, 14, 8, 15]. This electromagnetic dropping mechanism, depicted in the upper right corner of Figure 2, is modified to allow an initial forced rotation of the test object with an adjustable constant rotational frequency. In the beginning, the measurement chamber is in vacuum condition and the test object is held by an electromagnet located at the ceiling of the chamber. Before the flow is initiated, the model is accelerated to the target rotational frequency by a controlled stepping motor, that is connected to the magnet via a shaft with coupling. As soon as the free jet is initiated and stable, the model is released from the holder and falls in vacuum. When passing the top shear layer, the increasing total pressure causes an additional rotational component on the body, the angular velocity of which is less than the initial forced rotation. Subsequently, the effective test time of about 0.1 s begins as soon as the model is completely within the homogeneous core flow and ends as soon as it reaches the edge of the core flow. At the end, the model crosses the lower part of the shear layer before it is caught at the bottom of the test section.

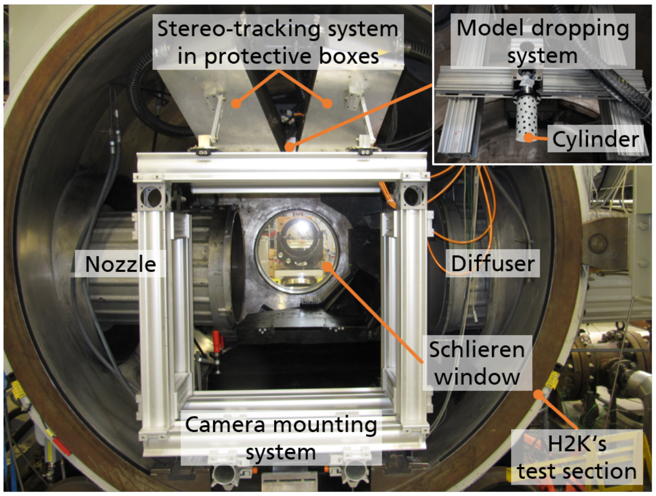

Fig. 2. Experimental setup with free-flight technique in H2K's test section

3. EXPERIMENTAL RESULTS OF AEROTHERMAL LOADS

The experimental results of the stationary and the cylinder rotating around its longitudinal axis with constant rotational frequencies of $f = \{0.8, 4, 8\}$ Hz are presented below for the two test conditions TC1 and TC2. Data from IR thermography and schlieren videography are available for all performed tests.

3.1. Surface temperature distribution

Surface temperature maps at TC1 are displayed in Figure 3, which were acquired at three different times after the flow reaches the stationary cylinder (at t_0). It should be noted that the circular points in the surface temperature representations are steel markers to be used for mapping and fusion of IR data. As can be seen in Figure 3, the temperatures and thus the heating rates on the lateral surface are particularly high at the cylinder's stagnation line, which is roughly in line with the double-point marker at the top left of the model. As expected, the surface temperature T decreases in streamwise direction from the stagnation region to the wake region. Additionally, it can be seen that the frontal area of the cylinder in particular heats up over time to about 220°C (at t_0 + 10 s).

3.2. Effect of rotation

The influence of cylinder rotation on the resulting surface temperature profiles is shown in Figure 4. Please note that the apparent temperature increases and decreases at the beginning and end of the extracted lines are due to the angular dependence of the emissivity of PEEK and need to be corrected for the data fusion. At first glance, the rotation of the cylinder leads to a more uniform temperature distribution compared to the stationary case at f = 0 Hz. As a result, the heat is distributed more homogeneously during rotation in all cases, which leads to lower temperatures in the stagnation region and higher temperatures further downstream compared to the stationary cylinder. A possible explanation for this might be that a fixed point on the cylinder is heated when rotating towards the incoming flow and cooled when facing the wake region. An implication of this finding is that the peak heat fluxes for rotating objects of space debris are significant lower than of stationary ones, which should be considered in the design process of D4D.

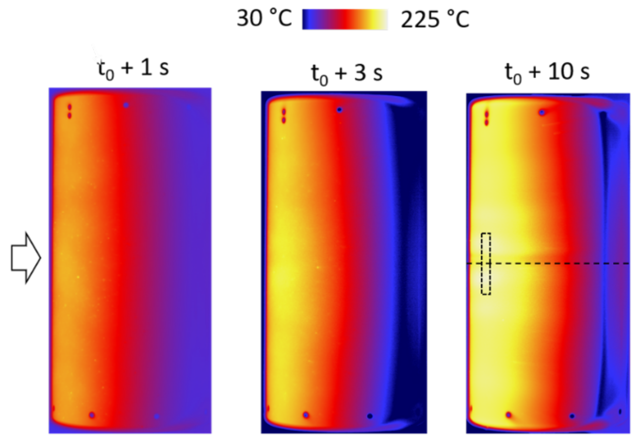

Fig. 3. Time series of the lateral surface's temperature distribution at TC1 with $\alpha = 90°$ and $f = 0$ Hz

Interestingly, the rotational frequency plays no role for the surface temperature distribution along a circumferential line at 10 s after start of flow (see right line chart of Figure 4) reaching a homogeneous temperature at almost the same level. In contrast to the longer heating phase, the configuration at 3 s after the start of flow with f = 0.8 Hz shows a still remarkable temperature gradient downstream of the stagnation point for the temperature profile in a weakened form compared to the stationary one, while the profiles at f = 4 Hz and 8 Hz are almost constant. These differences can be explained by the fact that all segments of the lateral surface were impinged more equally by all flow regions for the higher rotational frequencies after the short time with flow impact than for the lower rotational frequency. In conclusion, the higher the rotational frequency, the faster the homogenisation of the surface temperature in the transverse direction.

With the homogenisation of the surface temperature distribution shown above, it should be noted that the selected IR camera observes the region of the lateral surface that has just passed the wake due to its positioning. For this reason,

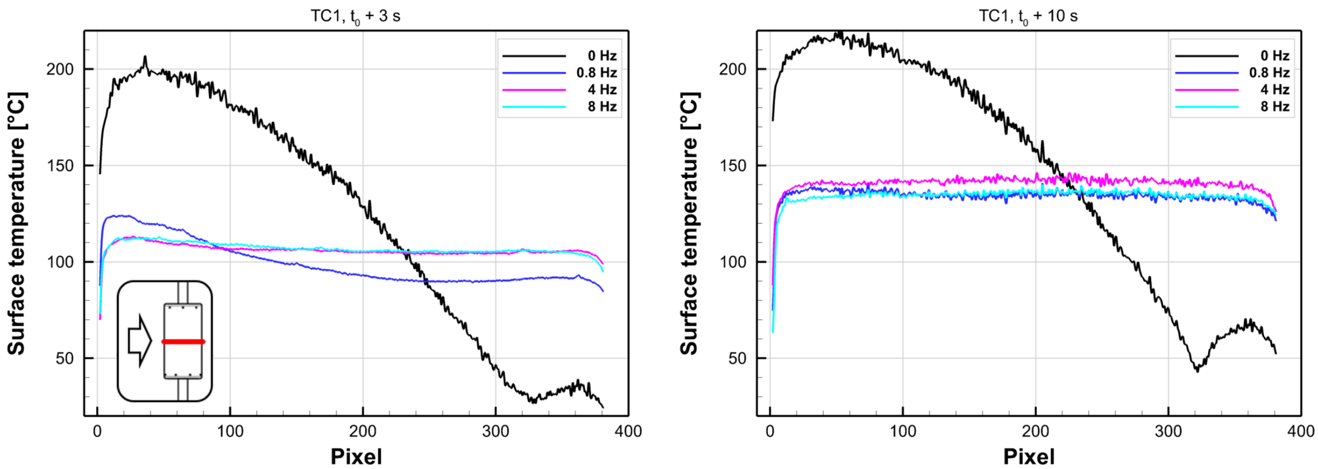

Fig. 4. Temperature profiles at TC1 for different rotational frequencies extracted 3 s and 10 s after start of flow

the temperature profiles appear different when the cylinder is rotated counter-clockwise, so that the profile changes from a constant trend to an increasing-decreasing trend in streamwise direction.

3.3. Stripe-like pattern

Interestingly, a stripe-like pattern in the transverse direction was found in the surface temperature representations of the rotating cylinder (see Figure 5), which was not observed in the stationary one. This flow phenomenon can be seen clearly in both surface temperature maps of Figure 5 for the free-stream Reynolds numbers based on the model diameter of 9.9×10^5 (TC1) and 2.6×10^5 (TC2), which were measured 11 s after start of flow. In addition, the surface temperature profiles are provided in Figure 5 when looking in the longitudinal direction parallel to the cylinder's axis. From this line chart, it is apparent that locally increased temperature levels arise, which dominate in the centre area of the cylinder. These increased temperature levels run in the transverse direction, with the stripes being parallel to each other. Of interest here is the significant impact of the Reynolds number on the structure and temperature difference between peak and trough of the stripe-like pattern. In doing so, the number of local peaks is higher and the temperature difference is lower for a lower Reynolds number than for a higher one. It is difficult to explain this result, but it might be related to Taylor-like vortices, which are an instability mechanism through the centrifugal force developing on sufficiently bended surfaces of rotating objects [16]. These flow features are also characterised as vortices, that are aligned with their axes parallel to the main flow direction.

Remarkable relationships can be seen with regard to the influence of single parameters. On the one hand, the rotational frequency and the direction of rotation have no significant influence on the stripe-like pattern under the test conditions investigated, while on the other hand the phenomenon disappears in the case of inclined configurations.

4. EXPERIMENTAL RESULTS OF AERODYNAMIC LOADS

In the following, the experimental results of the cylindrical bodies in free flight at TC2 and different initial pitch angles are presented, also analysing the initial-forced yaw rotation of the models in axial flow and the initial-forced roll rotation of the models in cross flow. Data from schlieren videography and stereo tracking including motion derivatives and aerodynamic coefficients are available for all conducted tests.

4.1. Effect of body shape and orientation

The drag force (C_D), lift force (C_L) and pitching moment coefficient (C_m) based on the experimental motion data from the stereo tracking are shown for the cylindrical bodies in Figure 6 as a function of the inclination of the model relative to the inflow, i.e. total angle of attack based on the angle of attack α (AoA) and the angle of sideslip β (AoS). It should be noted that the change in the AoA during the tests is induced by the effect of the free jet's shear layer, as explained in [13]. Additionally, experimental results of a previous work [8] with cylinders at various AoAs are also presented in Figure 6 for the purpose of validation. This comparison shows that the current data of the cylinder for all presented aerodynamic coefficients correspond very well with those of the previous test series and that the aerodynamic loads are significantly dependent on the AoA, as previously stated.

Concerning the effect of body shape, the aerodynamic coefficients of the dogbone and the nozzle (refer to Figure 7) are compared with those of the cylinder in Figure 6. Just like the cylinder, the models with cavities also show a dependence on the orientation, but with smaller variations over AoA. Especially for AoAs near 90°, the drag coefficient is significantly

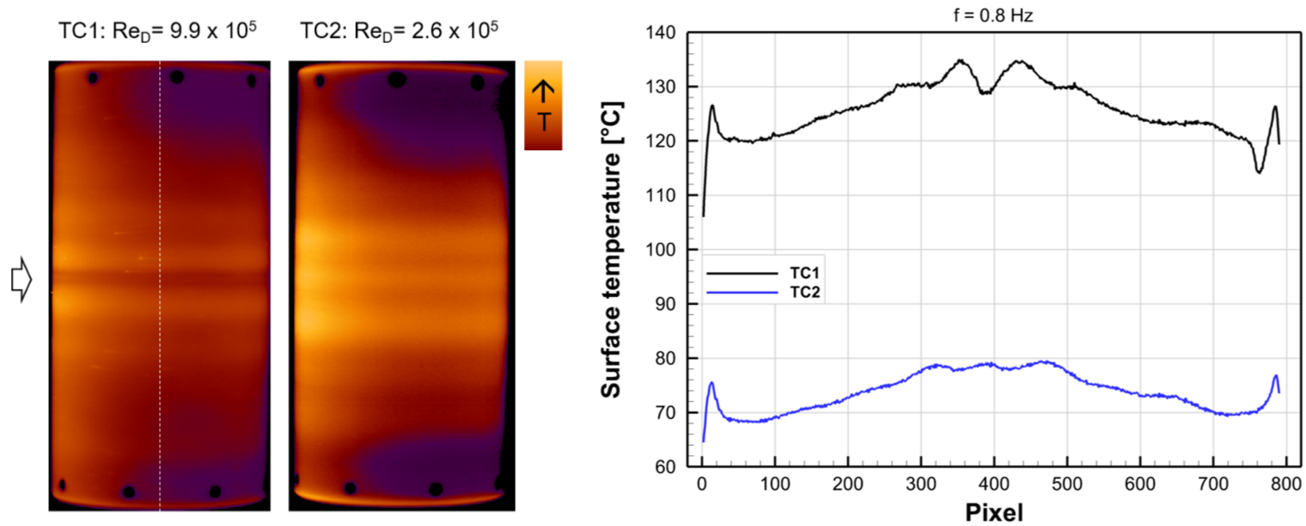

Fig. 5. Surface temperature distributions (left) and temperature profiles (right) of rotating cylinders for different Reynolds number with $\alpha = 90°$ and $f = 0.8$ Hz

lower, which can be attributed to a smaller frontal wetted area due to the cavity in the lateral surface. What also stands out in the present data is that the absolute drag and lift coefficients of the dogbone in the AoA range from 20° to 40° are higher than those of the nozzle. It is apparent from Figure 6 that the pitching moment of all bodies have a trim point at $\alpha = 0°$. In contrast to an unstable state for the cylinder, the geometries with a cavity in the lateral surface have a statically stable trim point here. This can be explained by the fact that the flow in the windward part of the cavity separates at its leading edge and reattaches upstream its trailing edge at low AoA. In doing so, the surface pressure in the rear part of the cavity is higher than in the front part, as the static pressure in the flow increases through a reattachment shock (see Figure 7). As a result, an opposing moment develops.

An interesting flow phenomenon was found in the schlieren images of Figure 7. These schlieren images present the flow topology of the nozzle body at different AoA. When examining the bow shock, a change in shape in front of the base surface can be observed for different AoA, which is an oblique shock with a small shock stand-off distance for high inclinations and a bended detached shock with a larger shock stand-off distance for low inclinations. This characteristic was also found for right circular cylinder (see [8]). However, a transition between these two states was observed for the nozzle in Figure 7, in which the shape of the bow shape in the stagnation region changes significantly and dynamically. In the course of this, the front part of bow shock, which initially has an oblique shape, is inflated and then deflated until the shock is completely detached. The observed transition of the bow shock could be attributed to a changing separation behaviour of the flow within the base cavity. Interestingly, the angle range of the bow shock's transition in the stagnation

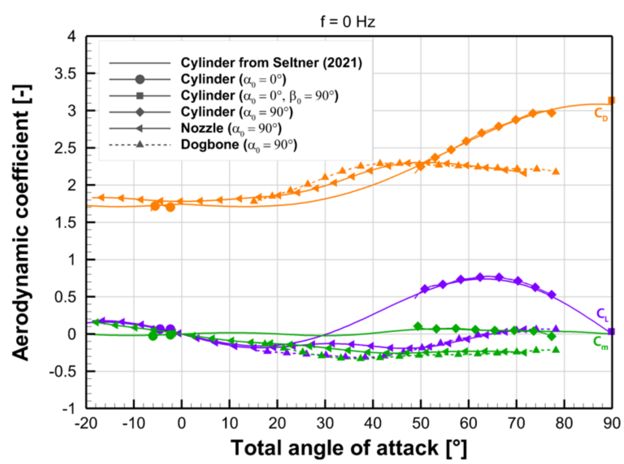

Fig. 6. Aerodynamic coefficients of different cylindrical bodies from several tests with different initial orientations as a function of total AoA compared to past cylinder experiments [8]

region correlates with the range of the deviations of force coefficients between the dogbone and nozzle body, as shown in Figure 6.

4.2. Effect of roll rotation

To analyse the effect of the roll rotation, cylinders at an initial AoA of 90° were initially rotated around their longitudinal axis, whereby a counter-clockwise (CCW) rotation is positive and is designated as "+" in the legends of the following figures. The motion of the models without initial rotation arises in an xz-plane and has just one variable angular displacement with the AoA, so that it is assumed to be 3DoF.

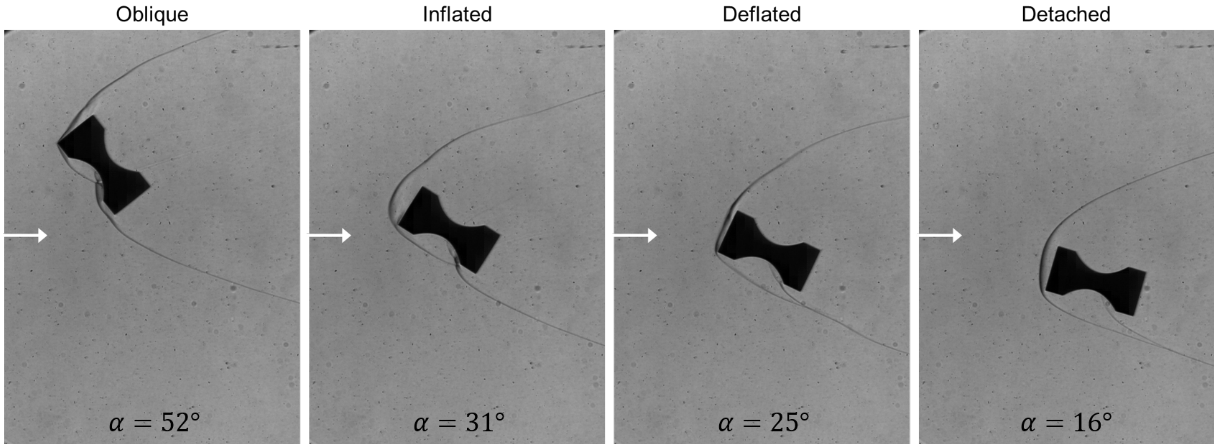

Fig. 7. Change in the bow shock's shape for a nozzle configuration with $\alpha_0 = 90°$ and $f = 0$ Hz in schlieren images

In contrast, the initial roll rotation causes an additional yaw rotation and spanwise displacement within the core flow, resulting in a 6DoF motion. Figure 8 presents the time series of the aerodynamic angles AoA and AoS for several cylinder configurations with different rotational frequencies and directions of rotation. What stands out in this line chart is that the rotational settings have a large influence on the evolution of AoA and AoS, with the deviations from the non-rotated cases increasing over time after entering the core flow. The decrease in AoA of cylinders with initial rolling is weaker than without initial rotation, whereby the differences become stronger at higher rotational frequencies and even cause a trend reversal. In doing so, the impact of the negative pitching moment due to the inhomogeneous total pressure distribution of the shear layer is counteracted by the rolling motion, resulting in a stabilising effect. However, it seems that the evolution of AoA is not affected by the direction of rotation. In contrast, the evolution of AoS depends significantly on the direction of the roll rotation. A positive roll velocity causes a negative change in the AoS, and vice versa. By increasing the absolute rotational frequency, the absolute change in AoS rises. These results are somehow surprising, because the circumferential velocity of the extreme case is significantly lower than the free-stream velocity having a relative difference of 0.15%.

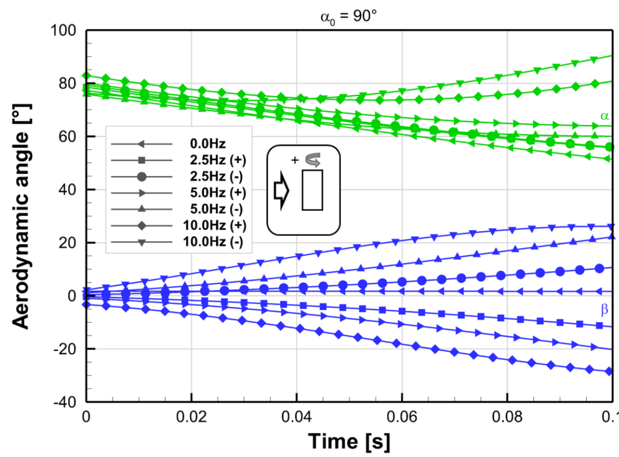

Fig. 8. Time series of the cylinder's aerodynamic angles AoA (green lines) and AoS (blue lines) with initial-forced roll motion at different rotational frequencies and directions of rotation

Up to this point, it is not clear whether this complex rotation is an aerodynamic effect or something else. However, a possible explanation for this might be the mechanical effect of precession, whereby a change in the orientation of the rotational axis occurs for rotating bodies as a result of an induced moment. For an exemplary test case with a rotational frequency of 2.5 Hz, the angular velocities of precession are determined based on the angular velocities and accelerations from measurements. In Figure 9, these angular velocities are compared with the values from the stereo tracking for the pitch and yaw components. It is apparent from this line chart that no significant differences were found between the velocities from measurement and precession calculation. Hence, these results suggest that the observed changes in AoA and AoS are due to a mechanical effect and that the aerodynamic effect of roll rotation is insignificant at the present frequencies.

Regarding the flight trajectories, no significant effect of the roll motion is apparent. The same applies to the corresponding aerodynamic force coefficients C_D and C_L, whereby they show good agreement with experimental data without initial rotation as a function of the total angle of attack. Taken together, these outcomes indicate that the effect of roll rotation on the aerodynamic loads is negligible at the current low rotational frequencies compared to the free-stream conditions.

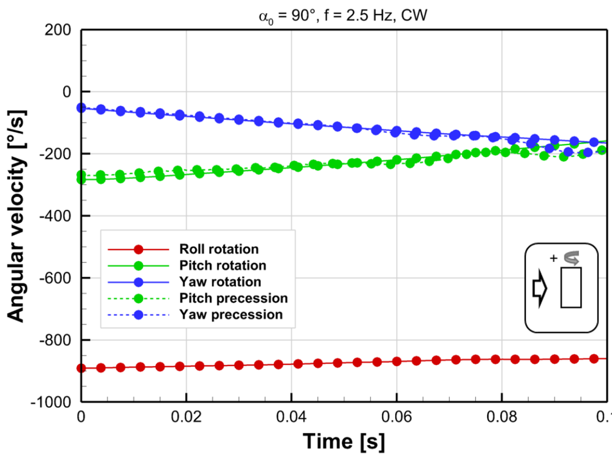

Fig. 9. Comparison of angular velocities from measurement and precession analysis for an exemplary test

4.3. Effect of yaw rotation

The effect of yaw rotation was studied by means of cylinders at an initial AoA of 0° being initially rotated around their normal axis. Figure 10 depicts flight trajectories of the cylinder with and without initial yawing in the xz-plane for different rotational settings. It is apparent from this line chart that the trajectories of initially yawing cylinders are largely between the curves of the initially fixed ones of $\alpha_0 = 0°$ and $\beta_0 = 90°$. This result is not surprising since the average frontal wetted area of the former with the base area is lower and that of the latter with the lateral surface area is higher than of the yawing configurations. One of the implications emerging from this finding is that an average trajectory can be assumed for yawing cylinders compared to non-rotated ones, regardless of the rotational settings.

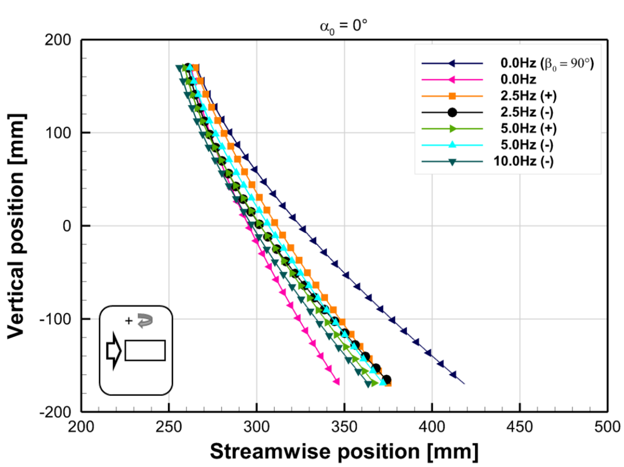

Fig. 10. Flight trajectories of the cylinder with initial-forced yaw motion at different rotational frequency and direction of rotation

As far as the rotational behaviour is concerned, small changes occur in the AoA and the roll angle over time, which are in the order of magnitude of up to 10° depending on the rotational frequency. These oscillations are also apparent in the graphs of the moment coefficients in Figure 11 for different rotational frequencies, where the aerodynamic coefficients for the rolling moment (C_l), pitching moment (C_m) and yawing moment (C_n) are presented. It is noteworthy that the frequency of pitching with 20 Hz is twice as high as that of rolling and yawing for the test case with an initial frequency of 10 Hz, for example. Several factors can explain this observation. First, the effect of precession also occurs in configurations with initial yawing as with rolling (see Section 4.2). Second, the yawing moment, that has an indirect effect on the AoA, features a period of 180° according to [8]. Both factors taken together may explain the doubling of frequency. Closer inspections at the rotational behaviour show that the motion of an initial yawing cylinder is much more complex, as continuous changes in AoS cause continuous changes in the yawing moment coefficient unlike the rolling configurations. In doing so, an interaction between the precession effect and the aerodynamic moments arises, whereby the angular velocities due to precession depend on the induced moments and the aerodynamic moments depend on the aerodynamic angles as a result of the prevailing angular velocities. Another result that stands out from Figure 11 is that the pitching coefficient is much higher than the yawing coefficient for the cylinder with initial-forced rotation. Thereby, maximum values of up to C_m = 0.7 are reached for the test with f = 10 Hz, which are nearly ten times higher than the maximum moment coefficient of the cylinder without initial rotation (see Figure 6). This observation is probably a result of the described interaction of precession and aerodynamics.

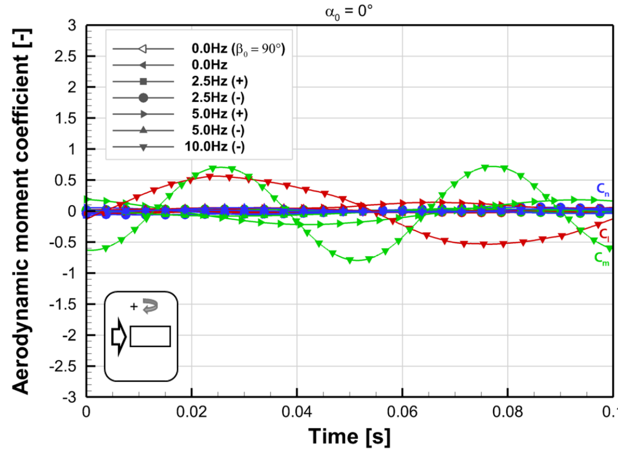

Fig. 11. Time series of the cylinder's moment coefficients C_l (red lines), C_m (green lines), C_n (blue lines) with initial-forced yaw motion at different rotational frequencies and directions of rotation

The aerodynamic and motion behaviour described above were also observed in the experiments of the cylindrical bodies with cavities.

5. CONCLUSION

In this study, the aero-thermodynamic effects that occur during the re-entry of rotating cylindrical bodies with concave and convex shapes into the atmosphere are analysed. At DLR's H2K in Cologne, two test series at Mach 7 were carried out with infrared measurements to examine the aerothermal loads and free-flight tests with stereo tracking to investigate the aerodynamic loads. Configurations with and without forced roll and yaw rotation were studied.

Broadly speaking, the experiments have shown that the rotation of the body leads to an averaging of the surface temperatures and the flight trajectory between the extremes. In doing so, the rotation causes a homogenisation of the surface temperature independent of the rotational frequency, so that the maximum temperatures and thus the peak thermal loads are reduced. For a constantly rolling cylinders in cross flow, this study has identified stripe-like patterns in the flow direction at the centre region of the lateral surface during the infrared measurements, which depend on the Reynolds number and are independent of the rotational frequency. The results of the free-flight tests indicate a precession motion for initially yawing or rolling cylinders as opposed to stationary ones, where the body undergoes a three-dimensional motion once the aerodynamic pitching moment is non-zero. However, no rotation-induced aerodynamic effects on the motion behaviour, such as the Magnus effect, were ascertained for the investigated configurations. Interestingly, an interaction between the torque-induced precession and the aerodynamic moment was found for the configuration with initial yaw rotation. Furthermore, an unexpected transition phase in the flow topology between oblique to detached bow shock was observed for the cylindrical bodies with a cavity in the base surface, whereby the shape of the bow shock first inflates and then deflates.

For future evaluation, it is planned to merge and analyse the infrared measurement data from all three cameras in order to carry out 1D heat transfer calculations for determining the heat fluxes and Stanton numbers.

6. REFERENCES

[1] ESA Space Debris Office, "ESA's annual space environment report," Tech. Rep. GEN-DB-LOG-00288-OPS-SD, European Space Agency, Darmstadt, Sept. 2023.

[2] ESA Space Mitigation Working Group, "ESA space debris mitigation requirements," Tech. Rep. ESSB-ST-U-007, European Space Agency, Darmstadt, Oct. 2023.

[3] Donald M. Kuehn, "Experimental and theoretical pressures on blunt cylinders for equilibrium and nonequilibrium air at hypersonic speeds," techreport NASA TN D-1979, Ames Research Center, Moffett Field, CA, United States, Nov. 1963.

[4] John F. McCarthy and Toshi Kubota, "A study of wakes behind a circular cylinder at M = 5.7," *AIAA Journal*, vol. 2, no. 4, pp. 629–636, Apr. 1964.

[5] R. K. Matthews and R. H. Eaves Jr., "Comparison of theoretical and experimental pressure and heat transfer distributions on three blunt nosed cylinders in hypersonic flow," techreport AEDCTR-67-148, Arnold Engineering Development Center, Arnold Air Force Station, Tennessee, June 1967.

[6] Mumoru Inouye, Joseph G. Marvin, and A. Richard Sinclair, "Comparison of experimental and theoretical shock shapes and pressure distribution on flatfaced cylinders at Mach 10.5," techreport NASA TN D-4397, Ames Research Center, Moffett Field, CA, United States, Feb. 1968.

[7] Gisu Park, Sudhir L. Gai, and Andrew J. Neely, "Laminar near wake of a circular cylinder at hypersonic speeds," *AIAA Journal*, vol. 48, no. 1, pp. 236–248, Jan. 2010.

[8] Patrick M. Seltner, Sebastian Willems, Ali Gülhan, Eric C. Stern, Joseph M. Brock, and Michael J. Aftosmis, "Aerodynamics of inclined cylindrical bodies free-flying in a hypersonic flowfield," *Experiments in Fluids*, vol. 62, no. 9, Aug. 2021.

[9] R. D. Klett, "Drag coefficients and heating ratios for right circular cylinders in free-molecular and continuum flow from Mach 10 to 30," techreport NASA TN D-1979, Ames Research Center, Moffett Field, CA, United States, May 1964.

[10] Thomas W. Rees, Tom B. Fisher, Paul J. K. Bruce, Jim A. Merrifield, and Mark K. Quinn, "Experimental characterization of the hypersonic flow around a cuboid," *Experiments in Fluids*, vol. 61, no. 7, June 2020.

[11] F.-J. Niezgodka, "Der Hyperschallwindkanal H2K des DLR in Köln-Porz (Stand 2000)," Tech. Rep., DLR, Köln, Jan. 2001.

[12] Dennis Daub, *Experimental investigation of supersonic fluid-structure interaction for future space transportation systems*, phdthesis, DLR/RWTH Aachen University, Cologne/Aachen, Sept. 2023, DLR-FB 2023-09.

[13] Patrick M. Seltner, Sebastian Willems, and Ali Gülhan, "Aerodynamic coefficients of free-flying cubes in hypersonic flowfield," *Journal of Spacecraft and Rockets*, vol. 56, no. 6, pp. 1725–1734, Nov. 2019.

[14] Paul J. Register, Michael J. Aftosmis, Eric C. Stern, Joseph M. Brock, Patrick M. Seltner, Sebastian Willems, Ali Gülhan, and Donovan L. Mathias, "Interactions between asteroid fragments during atmospheric entry," *Icarus*, vol. 337, no. 113468, Feb. 2020.

[15] Patrick M. Seltner, Sebastian Willems, and Ali Gülhan, "Aerodynamic interactions of blunt bodies free-flying in hypersonic flow," *Experiments in Fluids*, vol. 65, no. 80, May 2024.

[16] Geoffrey Ingram Taylor, "Stability of a viscous liquid contained between two rotating cylinders," *Philosophical Transactions of the Royal Society*, vol. 223, no. 605–615, pp. 289–343, Jan. 1923.